IOP Conf. Series: Earth and Environmental Science **163** (2018) 012084 doi:10.1088/1755-1315/163/1/012084

Very large eddy simulation of swirling flow in the Dellenback abrupt expansion tube

H Cheng[1,2], L J Zhou[1] and Y Z Zhao[2]

[1]College of Water Conservancy and Civil Engineering, China Agricultural University, No. 17 Tsinghua East Road 100083, Beijing, China

[2]Dongfang Electrical Machinery Co., Ltd., No. 188 Huang He West Road 618000, Deyang, Sichuan Province, China

lodgecheng@163.com

Abstract: There is usually a fluid dynamic phenomenon which involves a strong swirling flow between runner and draft tube of Francis turbines at part load condition. It is characterized by highly unsteady, large scale vortices, intense turbulence production, etc. The adverse pressure gradient in the draft tube cone can lead to vortex breakdown, which is recognized now as the main cause of hydro plant's instabilities. Therefore, it is very significant to predict the swirling flow field exactly in design period. However, the popular Reynolds-Averaged Navier-Stokes (RANS) or large eddy simulation (LES) method also has some shortcomings in CFD analysis, such as inaccurate large structures resolution or restrictive grid requirement. Very large eddy simulation(VLES), as a hybrid RANS/LES methodology, could combine the advantages of different turbulence approaches of RANS, LES, which has been proved by many authors. This paper presents a VLES case-study, based on the experimental studies of the swirling flow in the abrupt expansion by Dellenback et al. It is validated that VLES and LES model are much more accurate than the RANS models compared with test data. The standard k-ε and k-ω models are unable to accurately model the effect of the large-scale unsteadiness, while VLES almost has similar ability as LES in resolving that problem. In comparison with LES, it is demonstrated that VLES can give satisfactory convergence with a coarse mesh.

1. Introduction

Most hydraulic turbines are required to operate under wide range of loads in order to fulfill variable demands of an electrical grid. This often leads them to operate under part-load (off-design) conditions. There is highly unsteady and intense swirling flow in the draft tube cone, which often results in a precessing vortex. The adverse pressure gradient in the draft tube cone can lead to vortex breakdown, which is associated with large pressure fluctuations and flow instabilities. Nowadays, RANS and LES approaches are still the main methods for simulating turbulent flows in hydraulic turbines. Many authors have taken amount of researches in draft tube vortex using these two methods. Ruprecht et al [1], Scherer et al [2], Sick et al [3] and Ciocan et al [4] use k-ε and RSM models to calculate the pressure fluctuation caused by draft tube vortex and get a similar frequency with experiment results. However, the RANS method performs poorly in predicting the complex vortices and unsteady flow character. Though Guo et al [5], Wu et al [6] and Jošt et al [7] could predict intense vortex in draft tube by LES model, the request of mesh quality is extremely rigorous.

RANS-LES methodology, as a hybrid model, pursued by many researchers is to combine the computational efficiency of RANS in the near-wall regions with the fine accuracy of LES in large-scale turbulent structures. Speziale [8] rescaled a conventional RANS model through the introduction of a resolution control function F_r, which modeled the subscale turbulent stress tensor τ_{ij}^{sub} by damping the Reynolds stresses τ_{ij}^{RANS}. That could be expressed by the formulas below. β and n are the constant modeling parameters, Δ is the representative mesh spacing, L_k is the Kolmogorov length scale.

$$\tau_{ij}^{sub} = F_r \tau_{ij}^{RANS} \tag{1}$$

$$F_r = \left[1.0 - exp\left(\frac{-\beta\Delta}{L_k} \right) \right]^n \tag{2}$$

Hsieh et al [9] found that F_r could be written based on the turbulence energy spectrum and had a value between 0 and 1.0 with the final form below. L_c and L_i are the turbulent cut off length scale integral length scale respectively, which have different definitions in different models. Equation (3) constitutes the proposed VLES modeling of the new resolution control function F_r.

$$F_r = \min\left(1.0, \left[\frac{1.0 - exp\left(\frac{-\beta L_c}{L_k} \right)}{1.0 - exp\left(\frac{-\beta L_i}{L_k} \right)} \right]^n \right) \tag{3}$$

2. Turbulence models

The new VLES model was implemented in the general Computational Fluid Dynamics (CFD) code of ANSYS CFX , which is adopted for the numerical study. The VLES modeling are accomplished in the framework of the standard *k-ε* and *k-ω* turbulence RANS models.

2.1. VLES k-ε model

The original standard *k-ε* model includes turbulence kinetic energy *k* and dissipation rate *ε*.

$$\frac{\partial(\rho k)}{\partial t} + \frac{\partial}{\partial x_j}(\rho u_j k) = \frac{\partial}{\partial x_j}\left(\left(\mu + \frac{\mu_t}{\sigma_k} \right) \frac{\partial k}{\partial x_j} \right) + P_k - \rho\varepsilon \tag{4}$$

$$\frac{\partial(\rho\varepsilon)}{\partial t} + \frac{\partial}{\partial x_j}(\rho u_j \varepsilon) = \frac{\partial}{\partial x_j}\left(\left(\mu + \frac{\mu_t}{\sigma_\varepsilon} \right) \frac{\partial \varepsilon}{\partial x_j} \right) + \frac{C_{\varepsilon 1}\varepsilon}{k} P_k - C_{\varepsilon 2}\rho \frac{\varepsilon^2}{k} \tag{5}$$

P_k is the kinetic energy production and μ_t is the turbulent viscosity, as in equation (6) and (7).

$$P_k = \mu_t \left(\frac{\partial u_i}{\partial x_j} + \frac{\partial u_j}{\partial x_i} \right) \frac{\partial u_i}{\partial x_j} \tag{6}$$

$$\mu_t = C_\mu \rho \frac{k^2}{\varepsilon} \tag{7}$$

Compared with the standard *k-ε* model, the VLES *k-ε* model only modifies the formulation of the turbulent viscosity [10], as in equation (8).

$$\mu_t = F_r C_\mu \rho \frac{k^2}{\varepsilon} \tag{8}$$

There are some parameters associated with the function of F_r, in the form of

$$L_c = C_x(\Delta_x\Delta_y\Delta_z)^{1/3} \qquad L_i = \frac{k^{3/2}}{\varepsilon} \qquad L_k = \frac{\nu^{3/4}}{\varepsilon^{1/4}} \qquad C_x = \sqrt{0.3}\frac{C_s}{C_\mu} \tag{9-12}$$

C_s is the typical Smagorinsky LES model constant, all the constant modeling parameters as shown in table 1.

Table 1. Model constants for the VLES *k-ε* model.

β	n	C_μ	$C_{\varepsilon 1}$	$C_{\varepsilon 2}$	σ_k	σ_ε	C_s	C_x
0.002	2	0.09	1.44	1.92	1.0	1.3	0.1	0.61

2.2. VLES k-ω model

The original standard Wilcox *k-ω* model includes turbulence kinetic energy *k* and specific dissipation *ω*.

$$\frac{\partial(\rho k)}{\partial t}+\frac{\partial}{\partial x_j}\left(\rho u_j k\right)=\frac{\partial}{\partial x_j}\left(\left(\mu+\frac{\mu_t}{\sigma_{k1}}\right)\frac{\partial k}{\partial x_j}\right)+P_k-\beta'\rho k\omega \tag{13}$$

$$\frac{\partial(\rho\omega)}{\partial t}+\frac{\partial}{\partial x_j}(\rho u_j\omega)=\frac{\partial}{\partial x_j}[(\mu+\frac{\mu_t}{\sigma_{\omega 1}})\frac{\partial\omega}{\partial x_j}]+\alpha_1\frac{\omega}{k}P_k-\beta_1\rho\omega^2 \tag{14}$$

P_k is the kinetic energy production and μ_t is the turbulent viscosity, as in equation (15) and (18).

$$P_k=\mu_t|S|^2 \tag{15}$$

$$|S|=\sqrt{2S_{ij}S_{ij}}\qquad S_{ij}=\frac{1}{2}\left(\frac{\partial u_i}{\partial x_j}+\frac{\partial u_j}{\partial x_i}\right) \tag{16-17}$$

$$\mu_t=\rho\frac{k}{\omega} \tag{18}$$

Compared with the standard *k-ω* model, the VLES *k-ω* model only modifies the formulation of the turbulent viscosity [11], as in equation (19).

$$\mu_t=F_r\rho\frac{k}{\omega} \tag{19}$$

There are some parameters associated with the function of F_r, in the form of

$$L_c=C_x(\Delta_x\Delta_y\Delta_z)^{1/3}\qquad L_i=\frac{k^{3/2}}{\beta'k\omega}\qquad L_k=\frac{\nu^{3/4}}{(\beta'k\omega)^{1/4}} \tag{20-22}$$

$$C_x=\sqrt{0.3}\frac{C_s}{\beta'}\qquad C_s=\sqrt{\frac{\left[\left(C_{s,0}^2\Delta^2|S|\right)^2+\nu^2\right]^{1/2}-\nu}{\Delta^2|S|}}\qquad \Delta=(\Delta_x\Delta_y\Delta_z)^{1/3} \tag{23-25}$$

$C_{s,0}$ is the typical Smagorinsky LES model constant, all the constant modeling parameters as shown in table 2.

Table 2. Model constants for the VLES *k-ω* model.

β	n	β'	α_1	β_1	σ_{k1}	$\sigma_{\omega 1}$	$C_{s,0}$
0.002	2	0.09	5/9	0.075	2	2	0.1

3. Abrupt expansion tube case

This work presents a case-study, based on the experimental studies of the swirling flow in the abrupt expansion by Dellenback et al [12]. This test used the Reynolds number Re and swirl number S_r defined fellow to describe operated point.

$$Re=\frac{V_{in}*D}{\nu}\qquad S_r=\frac{1}{R}\frac{\int_0^R r^2V_tV_a dr}{\int_0^R rV_a^2dr} \tag{26-27}$$

V_{in} is bulk velocity, D is inlet radius and ν is kinematic viscosity. R is radius, r is radial position, V_t is tangential and V_a is axial velocity.

The abrupt tube's geometry is shown in figure 1. The computational domain is extended 2D upstream of the expansion and 10D downstream of the expansion. Due to the case of $Re = 30000$ and $S_r = 0.6$ yields similar flow conditions as those of a helical vortex rope in a hydro turbine draft tube operating at part-load, this paper would take the case for validation at Z/D=0.25, 0.50, 1.00, 2.00 and 4.00, as shown in figure 1.

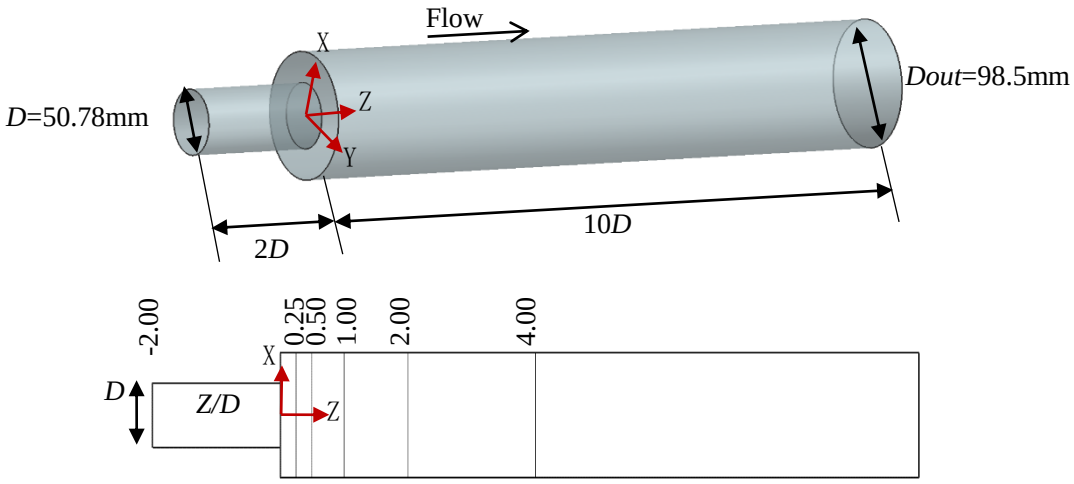

Figure 1. The Dellenback abrupt expansion geometry and measurement cross-sections.

3.1. Boundary condition and numerical settings

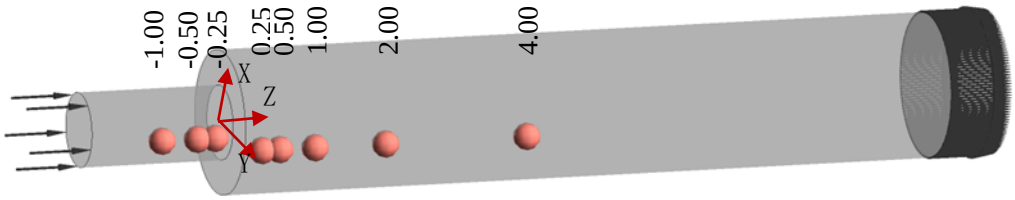

Figure 2. Computational domain.

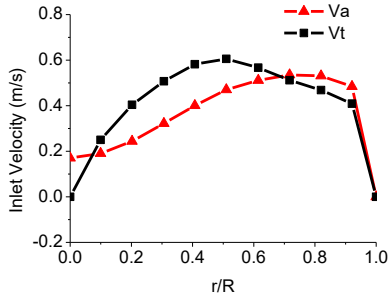

Figure 3. Velocity profiles on the inlet section.

The computational domain is shown in figure 2. At the inlet section the radial distributions of axial and tangential velocity components are obtainable from experimental measurements ($Re = 30000$ and $S_r = 0.6$), while the radial velocity is set to zero. Figure 3 shows the axial and circumferential velocity profiles applied to the inlet of the computational domain. For the outlet boundary condition, zero average static pressure is given at tube outlet. All wall surfaces are treated as no-slip wall to consider the friction loss.

This paper took five different turbulence models to compare with test results, including standard *k-ε*, standard *k-ω*, VLES *k-ε* and VLES *k-ω*, LES. The last three models would been calculated by unsteady type, using the steady results for initial value. In the simulation, the second order upwind scheme was used for discretization of convective term and the second order central scheme for discretization of diffusion term. The time term in the unsteady simulation was discretized by the second order backward Euler scheme. RMS residual type was chosen as convergence criteria, usually reaching to 1e-05 in most condition. In term of time step, it was chosen to assure a Courant-Friedrich-Lewy (CFL) number smaller than one in all cells, which was approximately $\Delta t = 0.0015s$. The unsteady simulations were considered to be converged when RMS residuals were also of the order of 1e-5 in each time step, which was run between 0-15 seconds, averaging the values from 10 seconds. All calculation was completed by the workshop computer with 56 processor cores of Intel Xeon.

3.2. Mesh scheme and grid scaling test

The computational domain was meshed by ANSYS ICEM software, and the O-grid block configuration is shown in figure 4. Six different grid densities (G1 to G6) were used to carry out the scaling test, as shown in table 3. The widely accepted grid convergence index (GCI) of Richardson extrapolation method was used to evaluate the numerical uncertainties and grid convergence. The extrapolation values and uncertainty in the grid convergence were estimated using the GCI method. The approximate and extrapolated relative errors as well as grid convergence index were estimated as in equation (28-30), and more details could be gotten from the reference [13].

$$e_a^{21} = \left| \frac{\phi_1 - \phi_2}{\phi_1} \right| \qquad e_{ext}^{21} = \left| \frac{\phi_{ext}^{12} - \phi_1}{\phi_{ext}^{12}} \right| \qquad \mathrm{GCI}_{fine}^{21} = \frac{1.25 e_a^{21}}{r_{21}^p - 1} \tag{28-30}$$

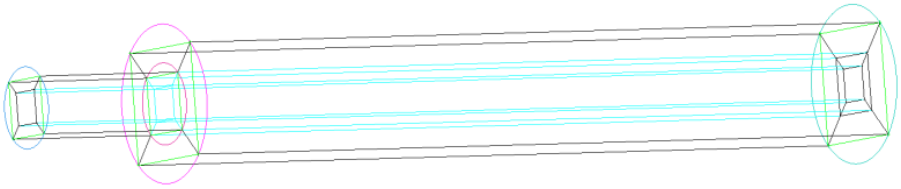

a) O-grid block

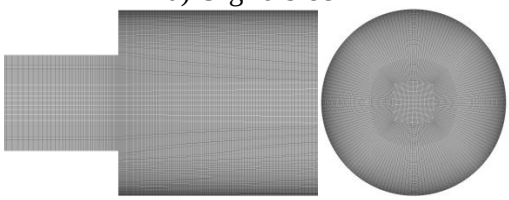

b) computational grid

Figure 4. mesh configuration.

The estimation was based on unsteady VLES *k-ω* and LES models with the time-averaged results. The critical parameter for the simulation was the velocity profile in section of 0.5*Z/D*. Figure 5 shows the velocity distribution for the different grids. The tangential velocity distributions of VLES *k-ω* for the different grids are almost similar, while the LES gets different trend for the location of maximal velocity with the increase of grids. In term of GCI index, VLES almost has a less value than LES in the whole grids, which proves that VLES has a better convergence and could give a satisfactory result with a coarse mesh, as shown in figure 6. Moreover, VLES G5 has a similar velocity distribution with LES G6 after abrupt expansion shown in figure 7, it could be concluded that VLES predicts exactly the turbulent flow flied with a coarse mesh and uses less time cost than LES. For the grid of G_6, the maximum extrapolated relative errors and grid convergence index of VLES were less than 3% and 3.5%, respectively. However, that indexes of LES could not reach the request of Richardson extrapolation method. Finally, G_6 was chosen to compare with the experimental measurements, whose Y^+ number was less than 26.

Table 3. Grid densities used in grid scaling tests

Grid type	G_1	G_2	G_3	G_4	G_5	G_6
Nodes	48712	103501	215616	427496	852816	2072176
Elements	46354	99736	209266	417696	837636	2048531
Element angle	⩾47.7	⩾46.5	⩾46.2	⩾45.7	⩾45.5	⩾45.6
Expansion factor	⩽2	⩽4	⩽3	⩽2	⩽3	⩽3
Aspect ratio	⩽41	⩽71	⩽41	⩽55	⩽49	⩽41
Y^+	⩽92	⩽60	⩽55	⩽41	⩽32	⩽26

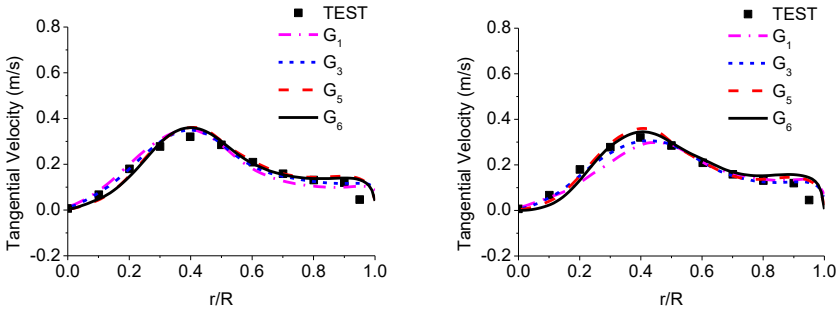

a) VLES b) LES

Figure 5. Tangential velocity distribution of different meshes (*Z/D*=0.5).

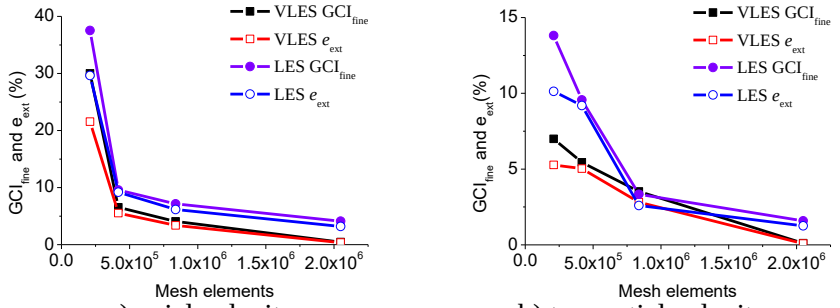

a) axial velocity b) tangential velocity

Figure 6. Averaged GCI index of different models (*Z/D*=0.5).

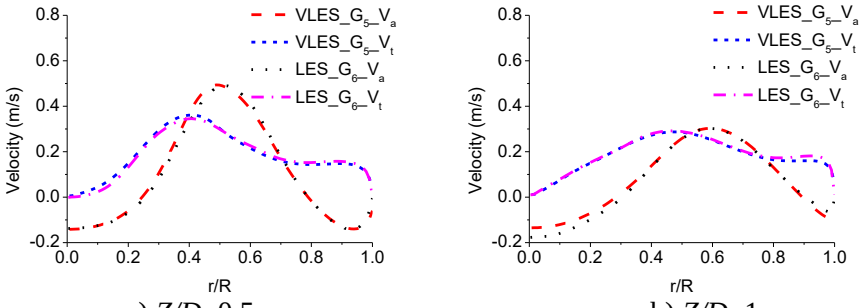

a) *Z/D*=0.5 b) *Z/D*=1

Figure 7. Velocity distribution of G5 G6 for VLES and LES.

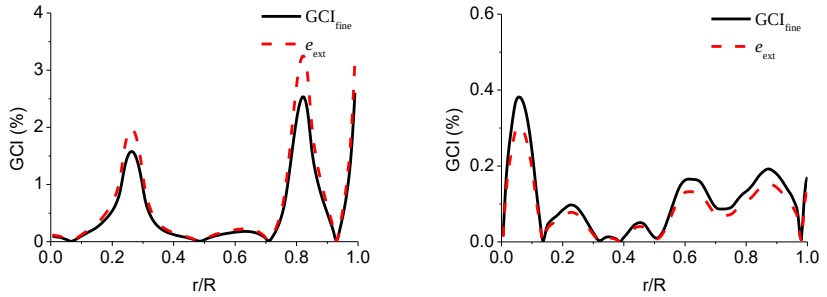

a) axial velocity b) tangential velocity

Figure 8. Discretization error and uncertainties GCI index analysis on section of *Z/D*=0.5 (VLES *k*-*ω*, G_6).

4. Results and discussion

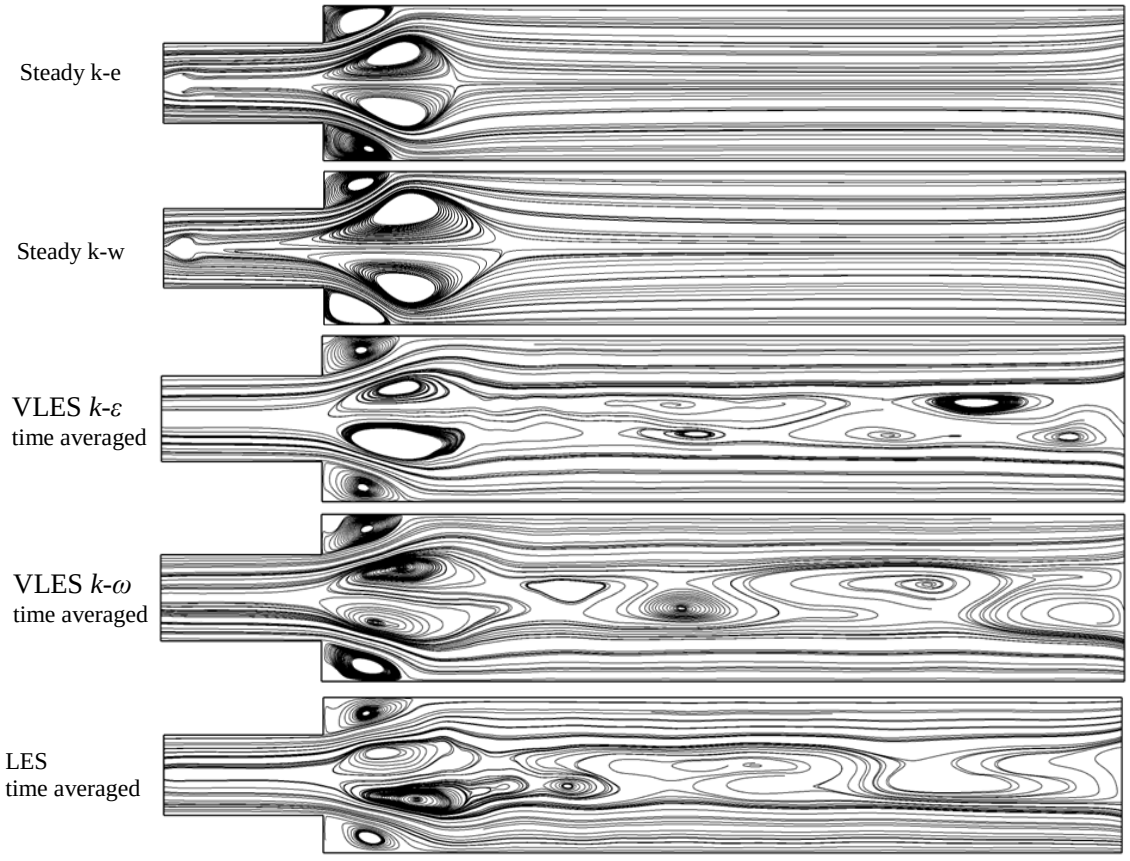

Figure 9. Streamline distribution on mid-plane.

Figures 9-11 show contour plots of the results on the mid-plane. Figure 8 shows the streamlines, and all turbulence models could predict a strong recirculation zone around the centerline and reversed recirculation zone near wall just downstream of the sudden expansion. It is a result that abrupt expansion area decreases the axial velocity and leads to a reversed velocity. It can be noted that steady RANS models are unable to capture the unsteadiness, as well as in transient mode. However, LES and VLES could simulate the large-scale vortices in the further downstream, which fits in with the fact.

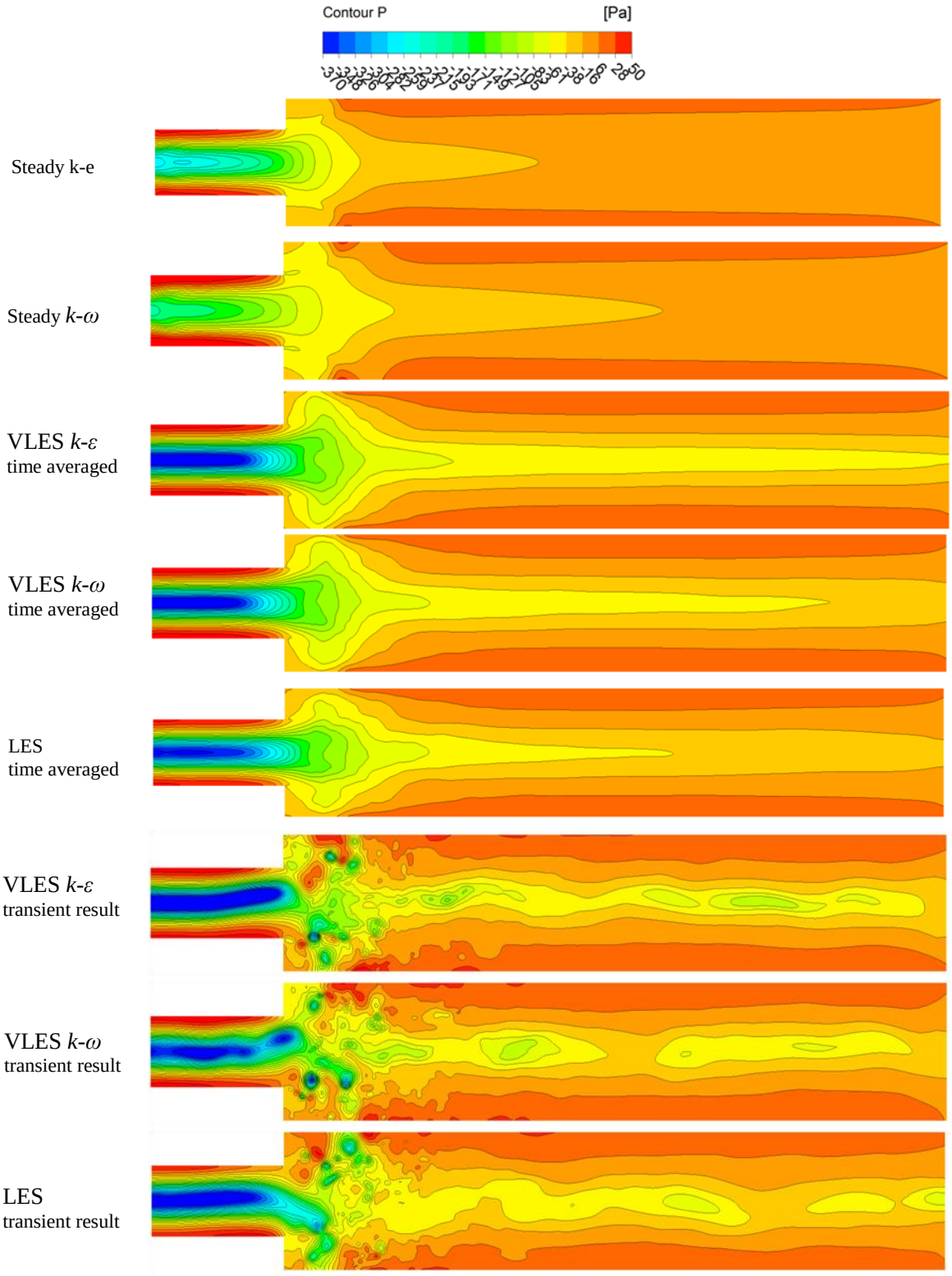

Figure 10. Static pressure distribution on mid-plane.

Figures 10-11 show the static pressure and velocity distribution at mid-plane. The results from standard *k-ε* and *k-ω* are quite similar. Turning to the LES and VLES cases, the flows seem to be well developed already at the inlet, and the central zone is much more clear with a thinner region of lower static pressure and higher velocity. Compared with LES and VLES, the main flow after expansion

calculated by RANS model is much closer to the tube wall, which is a notable difference among those models. What's more, the transient results reveal an unsteady vortex breakdown just after the abrupt expansion, followed by a quasi steady field further downstream. It is concluded that LES and VLES could simulate the intense turbulence flow well in the abrupt expansion tube.

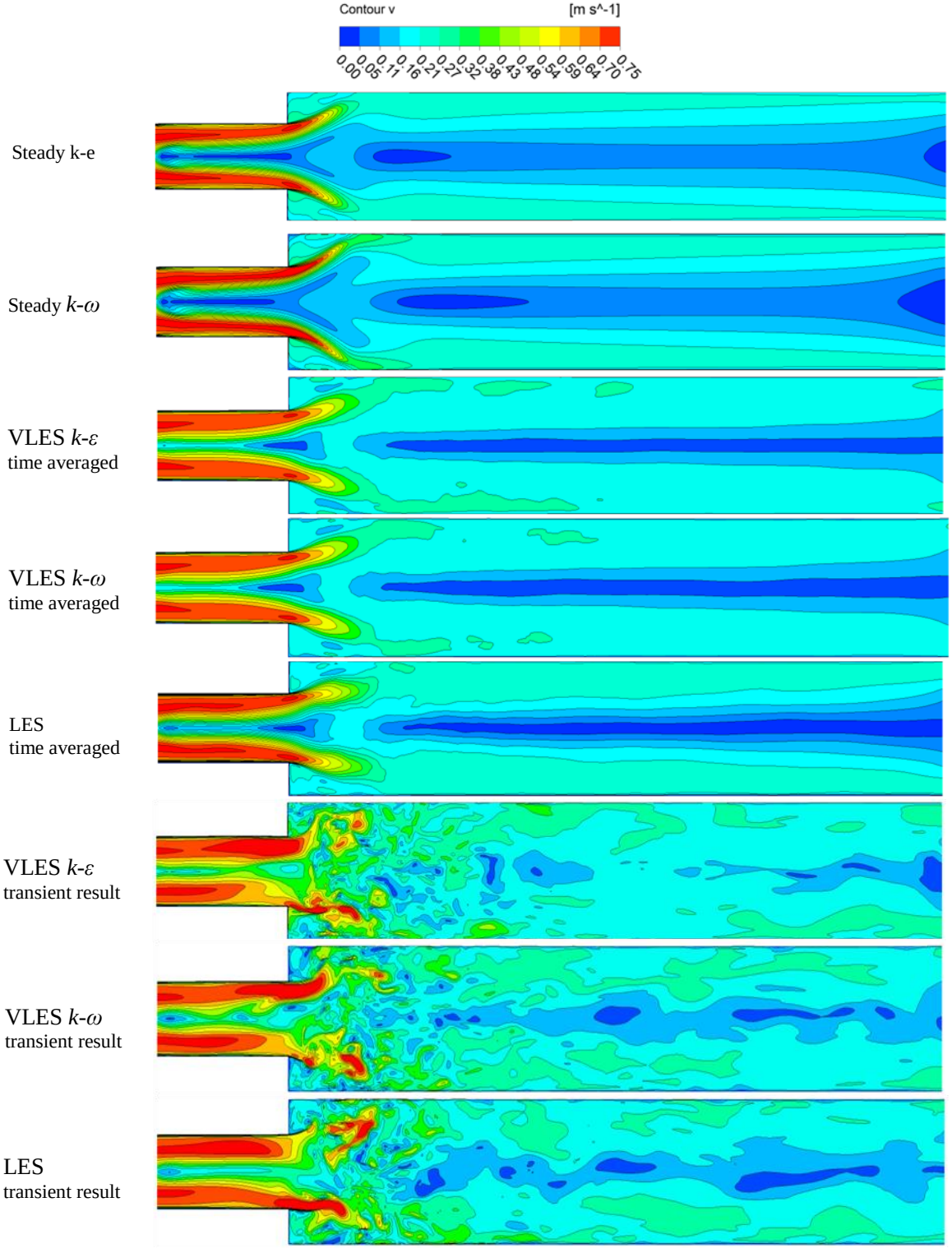

Figure 11. Velocity distribution on mid-plane.

a) Z/D=0.25

b) Z/D=0.5

c) Z/D=1

d) Z/D=2

e) Z/D=4

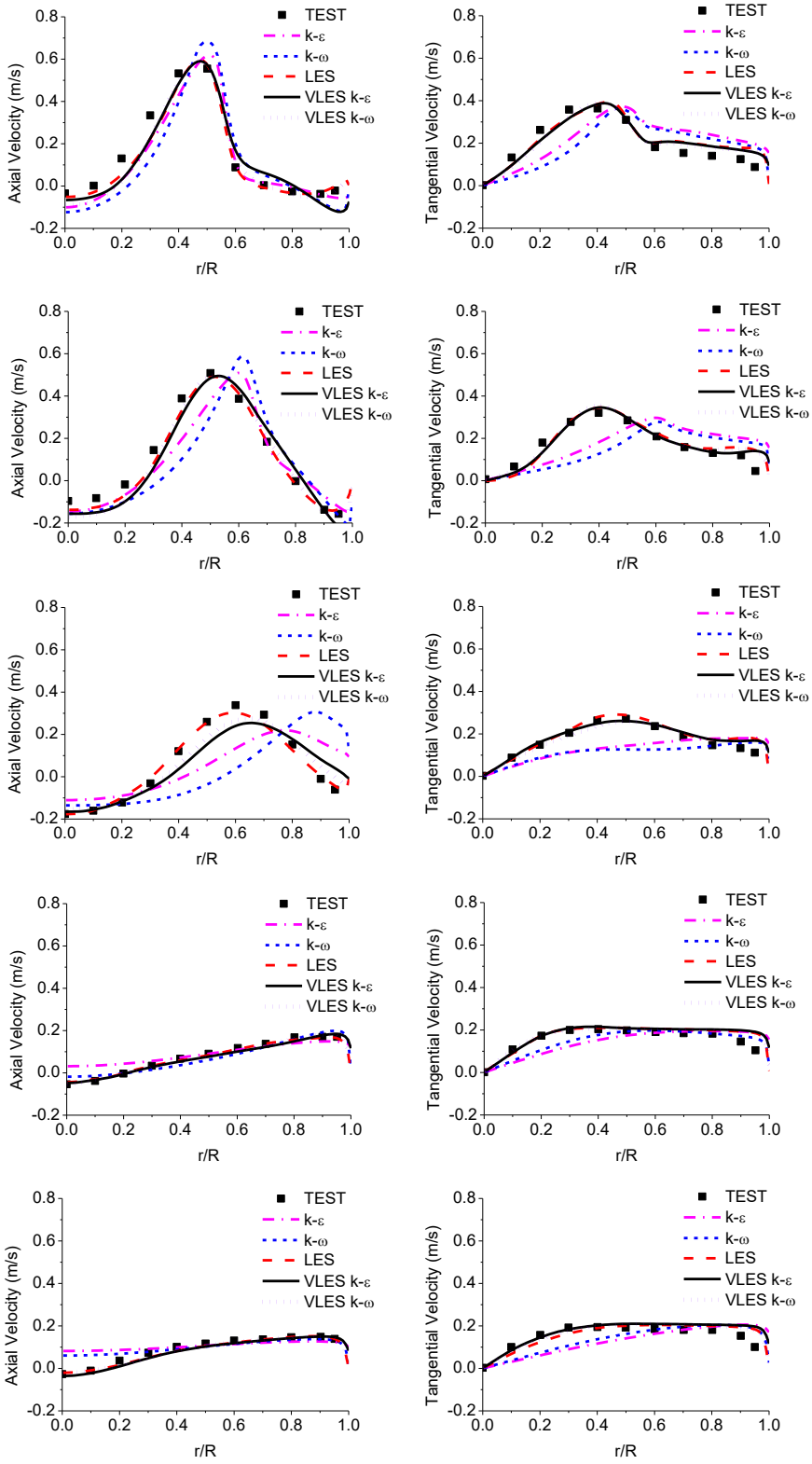

Figure 12. Axial and tangential velocity distribution on different sections.

Figure 12 compares the numerical axial and tangential velocity profiles with the experimental data at cross-section *Z/D*=0.25, 0.50, 1.00, 2.00, and 4.00. The X-coordinate represents the respective radial location of tube, and the value of Y-coordinate is the circumferential averaged velocity on such

sections. The test results present an on-axis recirculation region, whose maximal radius is about 0.3R at 1*Z/D* section with -0.2m/s axial velocity. RANS is almost not able to capture the main flow features with acceptable accuracy, and the location of maximal velocity offsets 01-0.2R compared with test results. The results from LES and VLES correspond quite well with the experimental data throughout the domain, though there are certain errors in the tube center before 1Z/D section. In addition, VLES *k-ω* could provide a better velocity profile near the tube wall than VLES *k-ε*, which proves that VLES *k-ω* is more appropriate to abrupt expansion flow.

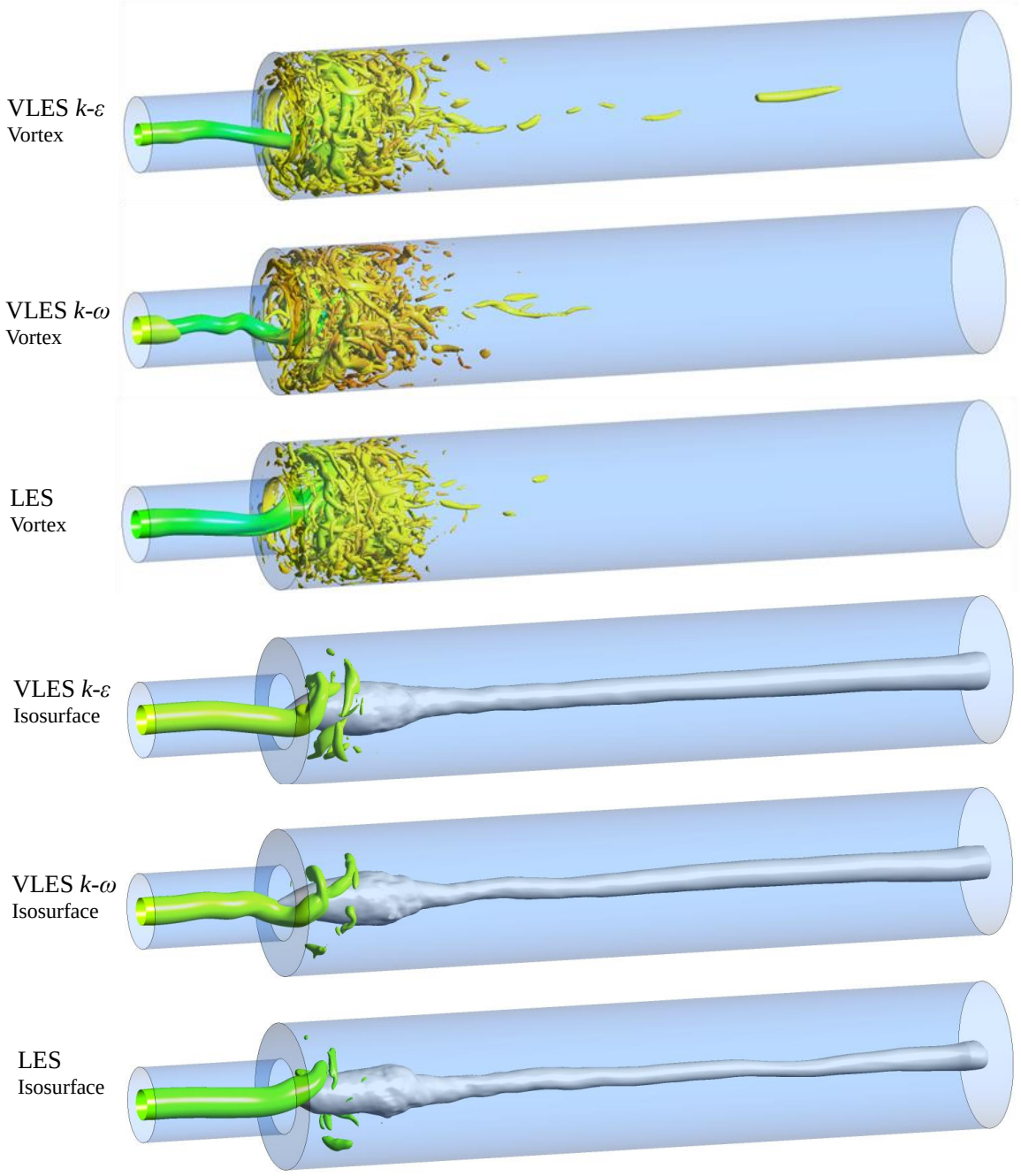

Figure 13. Snapshot of the vortex core visualized by λ_2=-2000s^{-2} in the first three pictures, and the main flow character shown by p=200Pa, V_a=0m/s.

A snapshot of the flow is presented in figure 13. The pressure isosurfaces of p=200Pa show that a helical vortex core is formed in the tube inlet and breaks down near the sudden expansion. The vortical structures could be well visualized by isosurfaces of λ_2=-2000s^{-2}. It is shown that the large helical

vortex twists with other counter-rotating small vortex structures formed in the near-wall, which almost disappears at the section of 3*Z/D* downstream. It could be found that the axis-symmetry stagnation zone, represented by isosurfaces of V_a=0m/s, is surrounded by helical vortex, which proves the Nishi's idea before [14].

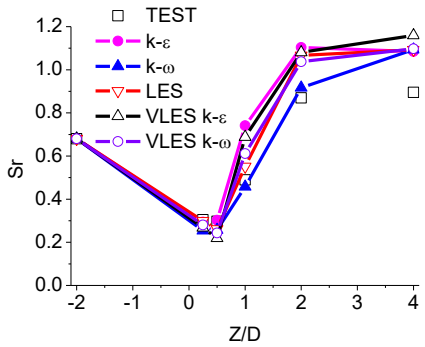

Figure 14. The evolution of swirling number from upstream to downstream.

In cases with the swirl number of different sections, as shown in figure 14, S_r decreases from 0.68 to 0.3 right after the expansion and then increases to 0.87 at *Z/D*=2 as well as the similar number at further downstream. Generally, this behavior can be related to the main flow trended to center of tube after expansion reduces the S_r value and the velocity distribution vanished by the bubble type vortex breakdown over the cross section gives higher S_r. All models could predict a similar trend with test results, but the values are always higher than test after the section of 1*Z/D*, as a result of the higher tangential velocity near wall.

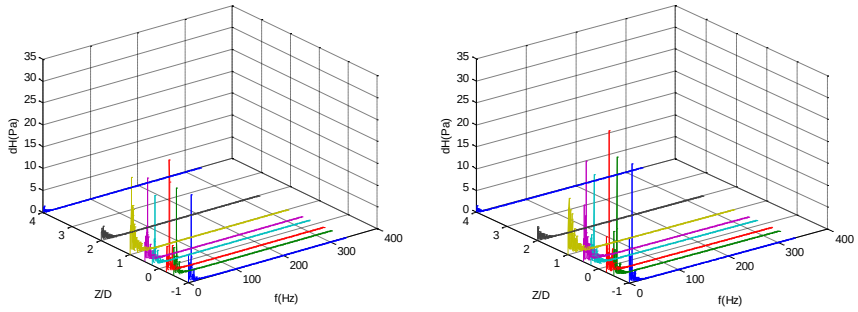

a) LES **b) VLES *k-ω***

Figure 15. The wall pressure fluctuations of different cross-sections.

The wall pressure fluctuations of cross-section *Z/D*=0.25, 0.50, 1.00, 2.00, and 4.00 are shown in figure 15. Time series of Fourier transform are 5000 time steps in length, corresponding to 7.5 seconds of real time. As can be seen, though the amplitude of pressure are somewhat larger from VLES, the results of LES and VLES k-ω are quite similar. The most distinct frequency is about 6Hz from -1*Z/D* to 0.5Z/D section, which may be the rotational speed of the helical vortex core according to some authors' point [15]. Moreover, there are clear low frequency near the expansion, which most likely correspond to the breakdown of large vortex structures in the recirculation zone near the wall. The amplitude of pressure decreases gradually from upstream to downstream, and sharply reduces after 1*Z/D* section. That is because the helical vortex breaks down after expansion and forms lots of small-scale vortices, which leads to the decay of the turbulence intense in the downstream.

5. Conclusions

Numerical simulation of turbulent flow in a abrupt expansion tube is performed in this study. Both steady and unsteady simulations are carried out using five different turbulence models, which is

compared with Dellenback experiment data. The regular RANS models can't simulate unsteadiness flow field caused by helical vortex ropes, while LES and VLES are able to capture the velocity, pressure distributions and wall pressure fluctuations after vortex breakdown. What's more, VLES could combine the advantages of different turbulence approaches of RANS, LES, and predicts the turbulent flow flied with a coarse mesh. It is a case-study for the draft tube rope vortex caused by the swirling flow of runner's outlet in hydraulic turbine at part load, and validated that VLES model would be quite potential in fluid machinery and other engineering applications.

Acknowledgements
The research presented in this work was supported by National Natural Science Foundation of China (NO:51479200).

References
[1] Ruprecht A, Helmrich T and Aschenbrenner T 2002 Simulation of vortex rope in a turbine draft tube *Proceedings of 21st IAHR Symposium on Hydraulic Machinery and Systems* Lausanne Switzerland.
[2] Scherer T, Faigle P and Aschenbrenner T 2002 Experimental analysis and numerical calculation of the rotating vortex rope in a draft tube operating at part load *Proceedings of 21st IAHR Symposium on Hydraulic Machinery and Systems* Lausanne Switzerland.
[3] Sick M, Dorfler P and Michler W 2004 Investigation of the draft tube vortex in a pump-turbine *Proceedings of 22nd IAHR Symposium on Hydraulic Machinery and Systems* Stockholm Sweden.
[4] Ciocan G D, Iliescu M S and Vu T 2007 Experimental study and unsteady simulation of the FLINDT draft tube rotating vortex rope *Journal of Fluids Engineering* volume129 pp146-158.
[5] Guo Y, Kato C and Miyagawa K 2006 Large eddy simulation of non-cavitating and cavitating flows in an elbow draft tube *Proceedings of 23rd IAHR Symposium on Hydraulic Machinery and Systems* Yokohama Japan.
[6] Wu X J, Liu S H and Wu Y L 2006 Helicity application on analyzing vortex rope in draft tube *Proceedings of 23rd IAHR Symposium on Hydraulic Machinery and Systems* Yokohama Japan.
[7] Jošt D and Lipej A 2011 Numerical prediction of non-cavitating and cavitating vortex rope in a Francis turbine draft tube *Journal of Mechanical Engineering* volume57 pp445-456.
[8] Speziale C G 1998 Turbulence modeling for time-dependent RANS and VLES: A Review *AIAA Journal* volume36 pp173-184.
[9] Hsieh K J, Lien F S and Yee E 2010 Towards a uniformed turbulence simulation approach for wall bounded flows Flow *Turbulence and Combustion* volume84 pp193-218.
[10] Han X S and Krajnović S 2013 An efficient very large eddy simulation model for simulation of turbulent flow *International Journal for Numerical Methods in Fluids* volume11 pp1341-1360.
[11] Han X S and Krajnović S 2015 Very-large-eddy Simulation based on k-ω model *AIAA Journal* volume4 pp1103-1108.
[12] Dellenback P A, Metzger D E and Neitzel G P 1988 Measurements in turbulent swirling flow through an abrupt axisymmetric expansion *AIAA Journal* volume6 pp669-681.
[13] Celik I B, Ghia U and Roache P J 2008 Procedure for estimation and reporting of uncertainty due to discretization in CFD applications *Journal of Fluids Engineering* volume7 pp1-13.
[14] Nishi M and Liu S H 2012 An outlook on the draft-tube-surge study *Proceedings of 26th IAHR Symposium on Hydraulic Machinery and Systems* Beijing China.
[15] Gyllenram W and Nilsson H 2008 Design and validation of a scale-adaptive filtering technique for LRN turbulence modeling of unsteady flow *Journal of Fluids Engineering* volume5 pp1-10.